# Study of the Geometrical Inaccuracy on a SPIF Two-Slope Pyramid by Finite Element Simulations

Carlos Felipe Guzmán[a,b,*], Jun Gu[c], Joost Duflou[d], Hans Vanhove[d], Paulo Flores[a], Anne Marie Habraken[b]

[a] *Universidad de Concepción, Departmento de Ingeniería Mecánica, Casilla 160-C, Correo 3, Ciudad Universitaria, Concepción, Chile*
[b] *Université de Liège, Department ArGEnCo, Chemin des Chevreuils, 1, 4000, Liège, Belgium*
[c] *Vrije Universiteit Brussel, Department of Mechanics of Materials and Constructions, Pleinlaan 2, 1050 Elsene, Belgium*
[d] *Katholieke Universiteit Leuven, Department of Mechanical Engineering, Celestijnenlaan 300B, 3001 Heverlee, Belgium*

**Abstract**

Single Point Incremental Forming (SPIF) is a recent manufacturing process which can give a symmetrical or asymmetrical shape to an undeformed metal sheet by using a relative small tool. In this article, a two-slope SPIF pyramid with two different depths, which suffers from large geometric deviations when comparing the intended and final shapes, is studied. The article goal is to detect if these divergences are due to new plastic strain while forming the second angle pyramid by using finite elements simulations. To validate the numerical results, both the shape and the forces are compared with experimental measurements. Then, an analysis of the material state is carried out taking the equivalent plastic strain, von Mises effective stress and

*Corresponding Author
*Email address:* cf.guzman@ulg.ac.be (Carlos Felipe Guzmán)
*URL:* www.argenco.ulg.ac.be (Carlos Felipe Guzmán)

yield stress distribution through a cut in the mesh. It is noticed that there is plastic deformation in the center of the pyramid, far from the tool neighbourhood. Also, high values of stresses are observed under the yield stress in other parts of the sheet. As a strong bending behaviour plus membrane tension is found in some sheet elements, these elastic stresses are due to a bending action of the tool. It is concluded that the main shape deviations come from elastic strains due to structural elastic bending, plus a minor contribution of localized springback, as no plastic deformation is observed in the angle change zone. Future developments in toolpath designs should eventually consider these elastic strains in order to achieve the intended geometry.
*Keywords:* Sheet Metal Forming, Single Point Incremental Forming, Finite Element Method, Deformation

## 1. Introduction

Incremental Forming refers to processes where the plastic deformation occurs by repeated contact with a small spherical tool. The small formed zone moves during the whole process, covering all the product and giving the final shape. The last decade has shown an increasing interest in Incremental Sheet Forming (ISF) processes. From early developments in Japan during 1990s, the research interest moved towards Europe coinciding with a massification of the CNCs machines and developments in CAD/CAM software products. A crucial aspect in the ISF processes is that the final shape is determined only by the tool movement. Many variations of ISF processes had been explored, from which the Single Point Incremental Forming (SPIF) and the Two Point Incremental Forming (TPIF) are the two most common ones. A review of

the technical developments of the process through the years can be found in Emmens et al. (2010). The focus of the article is the SPIF process, where a clamped sheet metal is deformed by using a relatively small spherical tool, which follows a complex path in order to get the required shape. A schematic representation of the process can be seen in Fig. 1, where the tool follows a path depicted in Fig. 2 for a conical shape.

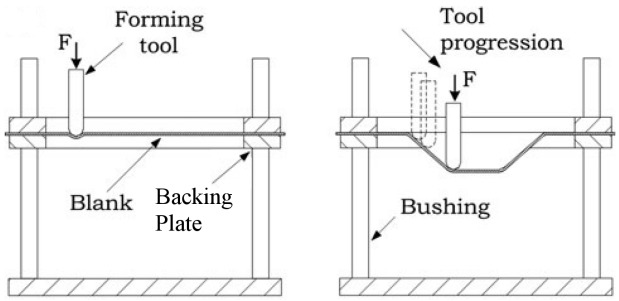


Figure 1: Schematic description of the SPIF (Henrard et al., 2010).

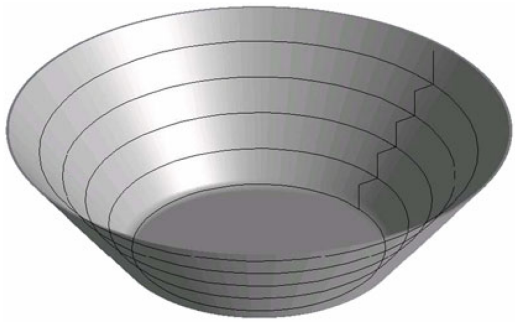

Figure 2: Toolpath for a conical shape (He et al., 2005).

One of the most prominent characteristics of the SPIF process it is the flexibility. Due to the fact that the shape is only given by the motion of the tool, no die is needed. Moreover, the toolpath can be easily controlled

by using a CAD/CAM software where a change of the final shape can be quickly and inexpensively done. This *dieless* nature makes the SPIF process appropriate for rapid prototyping, highly personalized pieces and other small batch shell-like structures, having a production cost lower than typical processes like deep drawing (Petek et al., 2007). A comprehensive review of the process characteristics and applications can be found in Jeswiet et al. (2005), ranging from dies manufacturing and automotive parts to medical applications (Ambrogio et al., 2005; Duflou et al., 2008b). In addition, the SPIF process has shown higher forming limits compared to other processes like stamping (Emmens and van den Boogaard, 2009).

The SPIF process, nevertheless, still has some important drawbacks. The poor geometrical accuracy represents a major disadvantage of the process (Jeswiet et al., 2005; Micari et al., 2007; Ambrogio et al., 2010), preventing a massive industrial acceptance (Allwood et al., 2005). Also the process slowness, due to feed rate limits in the CNC machines (Ambrogio et al., 2010), keeps the SPIF process away as an alternative for mass production. In order to improve accuracy many techniques have been proposed (Micari et al., 2007; Duflou et al., 2008a; Essa and Hartley, 2010). As pointed out by Micari et al. (2007), the best way to reduce inaccuracies is using a toolpath different from the target CAD profile in a way such that after the tool removal, the elastic springback and other deformations could bring the sheet to the desired shape. However, this approach requires a deep knowledge of the material behaviour of the sheet and the deformation mechanism occurring under the tool.

Despite the progress achieved during the last years, modelling the process through the Finite Elements Method (FEM) continues to be a demanding

task. Due to the small tool size and the still not clear deformation mechanism, a small size element mesh is required all over the sheet to achieve convergence and accuracy. Using an implicit scheme could get a high CPU time compare to an explicit one (Bambach et al., 2005), due the continuously alternating contact conditions. In general for explicit schemes, thanks to numerical methods like *mass-scaling* and/or *time-scaling*, it is possible to significantly reduce the computation time without a notable deterioration of the FE accuracy. Nevertheless, the search for the optimized scale values it is by no means trivial according to Henrard (2008). On the other hand, despite their higher simulation time, implicit schemes do not need *scaling* and they are unconditionally stable, i.e. their results do not depend on the mesh size (as long as it stays smaller than the tool radius) and the time step (automatically adjusted to get the equilibrium convergence). Implicit simulations show slightly better results in the geometry prediction than explicit schemes (Bambach, 2004).

The choice of the finite element is also important. Through Thickness Shear (TTS) has shown to be one of the most prominent characteristics of the SPIF process, contributing to the deviations between the sine law and the experimental results (Jackson and Allwood, 2009; Bambach, 2010) and explaining the high formability of the process (Eyckens et al., 2011), compared to other sheet metal processes like stamping and deep drawing (Filice et al., 2002). A comprehensive study of this phenomena requires the use of solid elements, but the simulation time could be extremely high even for simple geometries and toolpaths (Eyckens et al., 2010). In order to overcome this problem, techniques such as an adaptive remeshing (Lequesne et al.,

2008) and the substructuring approach (Hadoush and van den Boogaard, 2009) have been proposed for implicit simulations. Another way to reduce the computation time is by using shell elements (Hirt et al., 2002; Bambach and Hirt, 2005), but due to the element's limitations (i.e. 2D constitutive law and Kirchhoff-Love assumption) a correct description of the through thickness variables cannot be achieved. However, it is not the scope of this article to study the TTS and the process formability limits so it is possible to use a shell element.

With respect to material models, no major improvement is observed between the Hill and the von Mises yield locus for DC04 steel when predicting the geometry (Bambach and Hirt, 2005). Flores et al. (2007) and Henrard et al. (2010) reached the same conclusion for shape and forces prediction in aluminium AA3003. Nevertheless, both remarked that the hardening law has a strong influence. Henrard et al. (2010) proved that the Voce law is more suitable for force prediction for both bricks and shell elements, because it reaches a saturation level. For the strain prediction, Eyckens et al. (2010) indicates that the material model has little impact into the strains obtained from the FEM simulations.

In this paper, an analysis of the strain and stress fields during SPIF process is carried out using the FEM in two truncated two-slope pyramid, studied previously as a solar cooker application by Duflou et al. (2005). The research goal is to detect if the transition zone between the angles is affected by new plastic strain during the forming of the second angle, in order to understand the shape evolution and the amount of continuous springback throughout the process due to tool displacement and removal. The next

section describe the experimental measurements and section 3 presents the performed FEM simulations. Validation of the results by comparison of the predicted and measured shape and tool force is then provided in section 4. In section 5, strain and stress analysis are performed for reaching a better understanding of the process mechanism.

## 2. Experimental Setup

The experimental SPIF setup and measurement techniques are presented hereafter.

### *2.1. SPIF setup*

The SPIF is applied to an aluminium alloy AA3003 blank with initial dimensions 225 mm × 225 mm × 1.5 mm, supported on a four-sided steel basis fixture and clamped rigidly on this fixture by a 182 mm × 182 mm backing plate, as indicated in Fig. 1. Two truncated two-slope pyramids are formed, differing in the step-down size and consequently in their final depth. The geometry of both pyramids is depicted in Fig. 3. A three-axis MAHO CNC milling machine was used as the platform for the SPIF process. A cylindrical stylus with a 10 mm diameter spherical head was mounted on the horizontal axis of the machine, following the procedure outlined by Henrard et al. (2010). The whole fixture was mounted vertically on the working table of the milling machine so that the blank was perpendicular to the stylus (see Fig. 4).

During the forming process, the tool travels with a feed rate and only the material available inside of the orifice of the backing plate could be deformed by the tool. After travelling an entire path of one contour, the tool moved

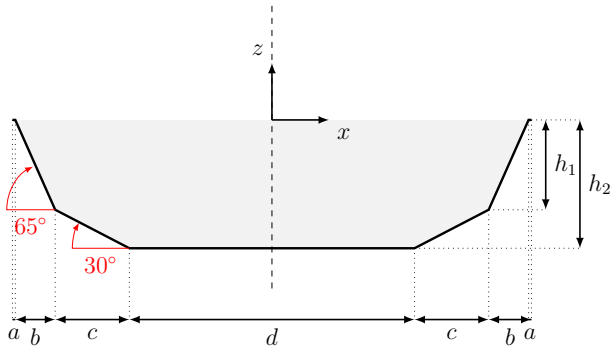


(a) Pyramid A

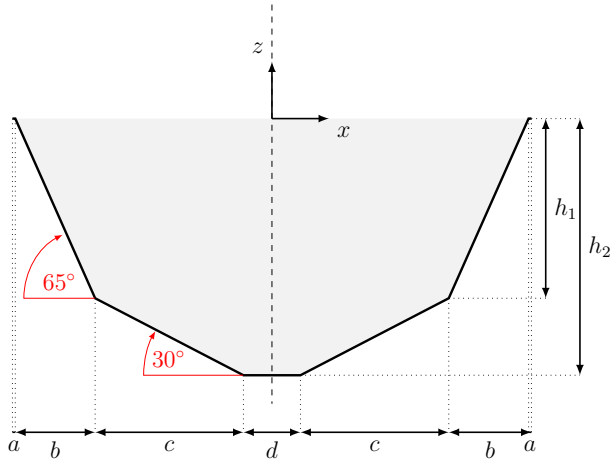


(b) Pyramid B

Figure 3: Profiles of the two pyramids (see the geometrical parameters in Table 2). The pyramid A has a step-down of 0.5 mm while the pyramid B 1.0 mm.

deeper in a stepwise fashion to follow the next contour until the desired depth is reached. The process parameters for this geometry can be seen in Table 1.

### *2.2. Experimental measurements*

The shape of the pyramid is measured by means of Digital Image Correlation (DIC) techniques. It consists of taking a sequence of pictures from

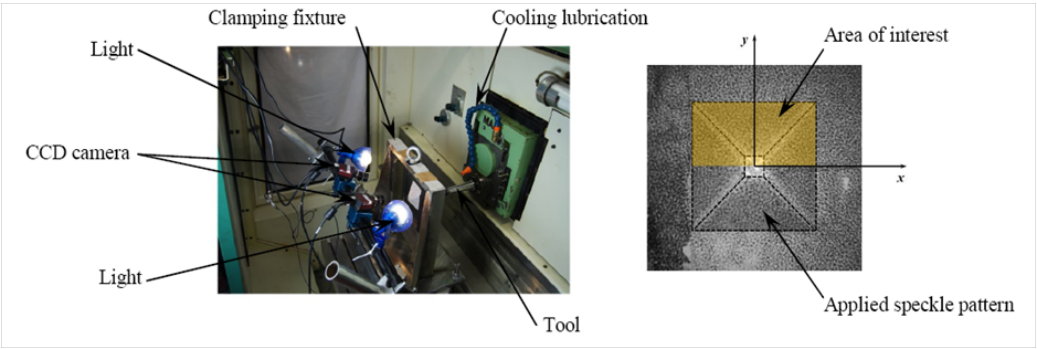


Figure 4: Experimental setup for the SPIF process and DIC measurements.

Table 1: Pyramid geometry and SPIF parameters.

| Geometry | Symbol | Value |
|---|---|---|
| Initial sheet thickness | $t$ | 1.5 mm |
| Wall angle 1 | $\alpha_1$ | 65° |
| Wall angle 2 | $\alpha_2$ | 30° |
| Number of contours 1 | | 63 |
| Number of contours 2 | | 27 |
| Step-down | $p$ | 0.5 mm and 1.0 mm |
| Tool diameter | $d_t$ | 10 mm |
| Tool feed rate | $v$ | 500 mm/min (DIC) and 1998 mm/min |

an object surface with two cameras (see Fig. 4) and then post-process each successive image. The tool feed rate is usually slower during the measuring as shown in Table 1. More details about the DIC technique used in this article can be found in Vasilakos et al. (2009) and Eyckens et al. (2010).

The reaction forces on the tool were measured using a force platform. The rig where the metal sheets are clamped is mounted with a six-component

Table 2: Geometry parameters of Fig. 3.

| Parameter | Pyramid A [mm] | Pyramid B [mm] |
|---|---|---|
| **a** | 1.0 | 1.0 |
| **b** | ≈14 | ≈28 |
| **c** | ≈26 | ≈52 |
| **d** | ≈100 | ≈20 |
| $h_1$ | 31.5 | 63 |
| $h_2$ | 45 | 90 |

dynamometer Kistler 9265B, measuring the orthogonal forces $F_x$, $F_y$ and $F_z$ (see Fig. 5). This setup was previously used by Aerens et al. (2009) and Henrard et al. (2010), and is able to measure a vertical force between -15kN and 30kN and two horizontal forces of ±15kN. It is possible to define an axial, radial and tangential force by looking at Fig. 5. The radial force is the force which points outward from the sheet during the tool movement, the tangential is positive following the tool displacement and the axial is perpendicular to the sheet plane.

## 3. FEM simulations

The LAGAMINE non-linear FEM code is used in the SPIF simulations. It is a lagrangian code developed by the ArGEnCo department of the University of Liège since 1980 (Cescotto and Grober, 1985). The code can simulate large displacements and deformations having available a large library of finite elements and constitutive laws.

### *3.1. Mesh description*

The undeformed finite elements mesh for a pyramid is shown in Fig. 5. 2016 nodes and 2102 shell elements are used to model the blank. Due to the

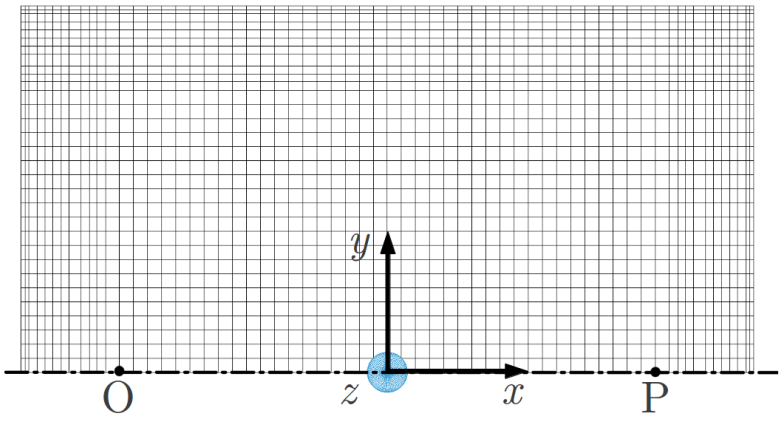


Figure 5: Initial mesh and tool position for the pyramid simulation in LAGAMINE.

symmetry, only half of the sheet is meshed. Rotational boundary conditions are imposed by a link between the displacements along the symmetry axis for the 6 degrees of freedom (Bouffioux et al., 2010; Henrard et al., 2010). Hence, the nodes O and P in Fig. 5 follows Eq. 1 for the displacements and Eq. 2 for the rotations.

$$(u_x)_O = -(u_x)_P \qquad (u_y)_O = -(u_y)_P \qquad (u_z)_O = (u_z)_P \tag{1}$$

$$(\phi_x)_O = -(\phi_x)_P \qquad (\phi_y)_O = -(\phi_y)_P \qquad (\phi_z)_O = (\phi_z)_P \tag{2}$$

Where $u$ is the vector of nodal displacements and $\phi$ the vector of nodal rotations. The nodes along the sheet edges are fixed in all three translations and rotations.

### *3.2. Toolpath*

The definition of the toolpath for the simulation should be as close as possible to the experiments, but some simplifications are introduced. For instance, the forming tool is modelled as a rigid sphere and a Coulomb friction coefficient of 0.05 was used in all simulations. As no time-dependent law is considered, the simulation time is different compared to the real process to decrease the CPU time. Fig. 6 depicts the toolpath seen from the top, with each tool position defined in Table 3. The tool center at the beginning of the first contours are specified in Table 4, because it is non linear. The explanation for this is that due its diameter, the tool could eventually *touch* the backing plate, which is avoided defining a non linear path. In both pyramids A and B, the change of angle from 65° to 30° occurs after contour 63 (at 630 s, because every contour lasts 10 s). The simulation is completed after the tool removal (unloading step) at 901 s.

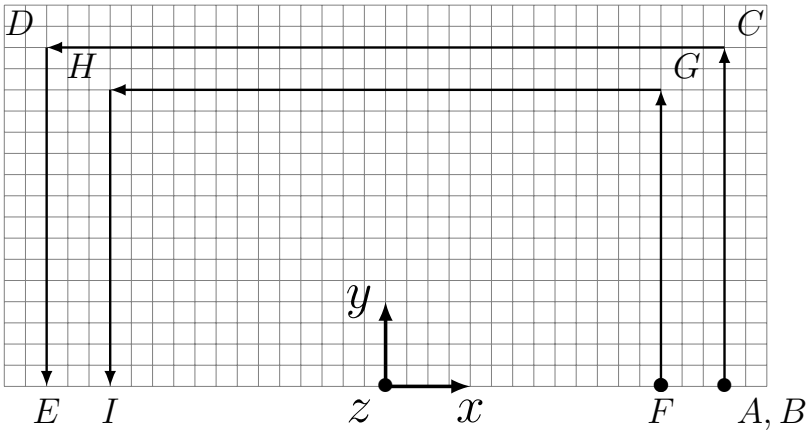


Figure 6: Tool motion during two successive contours. The letters represents the tool position at different times, as defined in Table 3.

Table 3: Tool position during the simulation. The depth depends on the step-down being different for pyramid A and B. The $x$ coordinate is defined in Table 4.

| | Time (s) | Position | Depth | $x$ (mm) | $y$ (mm) |
|---|---|---|---|---|---|
| **Contour 1** | 0 | A | 0 | X1 | 0 |
| | 1 | B | $p$ | X1 | 0 |
| | 3.25 | C | $p$ | X1 | Y=X1 |
| | 7.75 | D | $p$ | -X1 | Y=X1 |
| | 10 | E | $p$ | -X1 | 0 |
| | 10.01 | B | $p$-1 | X1 | 0 |
| | 10.02 | B | $p$ | X1 | 0 |
| **Contour 2** | 11 | F | 2*$p$ | X2 | 0 |
| | 13.25 | G | 2*$p$ | X2 | Y=X2 |
| | 17.75 | H | 2*$p$ | -X2 | Y=X2 |
| | 20 | I | 2*$p$ | -X2 | 0 |
| | 20.01 | F | 2*$p$-1 | X2 | 0 |
| | 20.02 | F | 2*$p$ | X2 | 0 |
| | ⋮ | ⋮ | ⋮ | ⋮ | |
| **Unload** | 900 | ... | 90*$p$ | -X90 | 0 |
| | 901 | ... | 90*$p$-3 | -X90 | 0 |

### *3.3. Finite element*

The COQJ4 shell element (Jetteur and Frey, 1986) is a 3D quadrilateral element with four nodes, based on Marguerre (1935) shallow shell theory and with 6 degrees of freedom in each node. It has successfully been used in SPIF

Table 4: $x$ coordinate of the tool center during the simulation.

| $x$ coordinate | Value (mm) |
|---|---|
| X1 | 87.821 |
| X2 | 87 |
| X3 | 86.429 |
| X4 | 86 |
| X5 | 85.67 |
| X6 | 85.67 |
| X7 | 85.1828 |
| ⋮ | ⋮ |
| X63 | 72.1262 |
| X64 | 71.2601 |
| ⋮ | ⋮ |
| X90 | 48.7435 |

simulations by Duflou et al. (2008b), Bouffioux et al. (2010), Henrard et al. (2010) and Eyckens et al. (2010), showing a good compromise between speed and accuracy. Each COQJ4 element is coupled with a contact element using a penalty approach (Habraken and Cescotto, 1998). The contact pressure is computed at four in-plane integration points by taking into account a penalty coefficient and penetration of the tool within the sheet.

### *3.4. Constitutive laws*

The material law used for the AA3003 material is elastoplastic with mixed isotropic-kinematic hardening. The elastic range is described by the Hooke's law with a Young's modulus $E$ =72 600 MPa and Poisson's ratio $\nu$ =0.36,

whose values were determined using an acoustic method performed at Vrije Universiteit Brussel. For the plastic part, the von Mises yield locus is used in this article:

$$F_{VM}(\sigma) = \frac{1}{2}\left[(\sigma_{11}-\sigma_{22})^2 + (\sigma_{11}-\sigma_{33})^2 + (\sigma_{22}-\sigma_{33})^2 + \ldots \right.$$
$$\left. \ldots + 2{\sigma_{12}}^2 + 2{\sigma_{13}}^2 + 2{\sigma_{23}}^2\right] - {\sigma_Y}^2 = 0 \quad (3)$$

where $\sigma_{ij}$ are the stress tensor components and the yield stress $\sigma_Y$ is a material parameter. For the isotropic hardening, the Voce law is used:

$$\sigma_Y(\epsilon^P) = \sigma_{Y0} + K(1 - \exp(-n\epsilon^P)) \quad (4)$$

where $K$, $n$ y $\sigma_{Y0}$ are material parameters. For the kinematic hardening, $\sigma$ in Eq. 3 is replaced by the *effective stress* $(\sigma - \alpha)$, where $\alpha$ is the *back-stress*. The Ziegler's equation describes the evolution of the *back-stress*:

$$\dot{\alpha} = C_A \frac{1}{\sigma_Y}(\sigma - \alpha)\dot{\epsilon}^P - G_A \alpha \dot{\epsilon}^P \quad (5)$$

where $C_A$ is the initial kinematic hardening modulus and $G_A$ is the decreasing kinematic hardening rate when the equivalent plastic strain rises.

The accuracy of the FEM predictions rely not only on the material model used but also on the identification procedure. In this article, an inverse method is used to fit material data. This method couples the LAGAMINE simulations with shell elements to determine the material parameters of a material law (i.e. von Mises yield locus, Voce and Ziegler hardening). The experiments used are the tensile, monotonic and Bauschinger shear test and also an indent test (Henrard et al., 2010). The final set of parameters used in the simulations is presented in Table 5.

Table 5: Set of material parameters for the SPIF simulation.

| Isotropic Hardening | | Kinematic Hardening | |
|---|---|---|---|
| Voce | | Ziegler | |
| $K$ | 89.0 | $C_A$ | 89.0 |
| $\sigma_0$ | 20.0 | $G_A$ | 0 |
| $n$ | 22.5 | | |

## 4. Validation of FEM simulations

To validate the FEM simulations, both the shape and the force predictions are compared with experimental results. The experimental shape is extracted from the pyramid B while for the forces, the pyramid A is used.

### *4.1. Shape validation*

22 material points in a cut through $x = 0$mm in the undeformed sheet (see Fig. 3), starting from $y = 0$mm and ending in $y = 75$mm, are selected and their $z$ positions measured. The experimental and numerical results are depicted in Fig. 7. They are extracted at the end of five different contours, just before the tool is lifted to move to another contour (point E and I in Fig. 6). It should be noted that the numerical and experimental curves are intentionally shifted to coincide at $y = 80$mm, $z = -10$mm. The reason is that near the backing plate it is very difficult to extract data, and there is no accurate information about the shape between $y = 75$mm and $y = 90$mm. This *transition zone* between the clamped part and the pyramid wall has been considered previously by Eyckens et al. (2010). The DIC also cannot retrieve information about the point near $y = 0$mm at the end of the process.

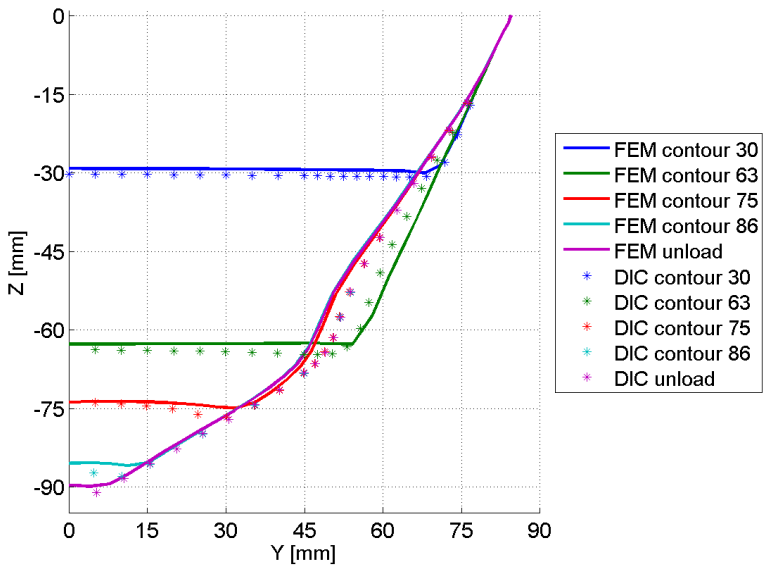


Figure 7: Comparision between experimental and numerical curves in different contours for pyramid B. The selected experimental points and mesh nodes corresponds to a cut along $x = 0$ in the undeformed mesh.

The numerical results in Fig. 7 follow the overall shape of the experimental pyramid. However, there are some differences due to different sources of error. For instance, DIC points do not stay exactly at $x = 0$mm during the process because the *twist effect* displaces the points at the $x$ coordinate. The twist is an unwanted deformation due to the combined effect of tangential forces induced by the unidirectional contouring toolpath and sheet thinning (Duflou et al., 2010). Nevertheless, this phenomena does not significantly affect the final shape, because the maximum nodal displacement in the tangential direction it is around 1.2 mm in Fig. 8, while the length of the cut is 90 mm. Another factor is that the shape prediction at the unload step seems better than the others contours, probably due to small differences in

the contour definition between the FEM simulation and DIC measurements. Nevertheless, considering the high wall angle of the 65° pyramid, the TTS is probably the major source of deviations between the shell predictions and the experiments, as TTS increases with the drawing angle. As explained by Henrard et al. (2010) in a cone with a draw angle of 20°, the TTS is negligible while for 65° it is large.

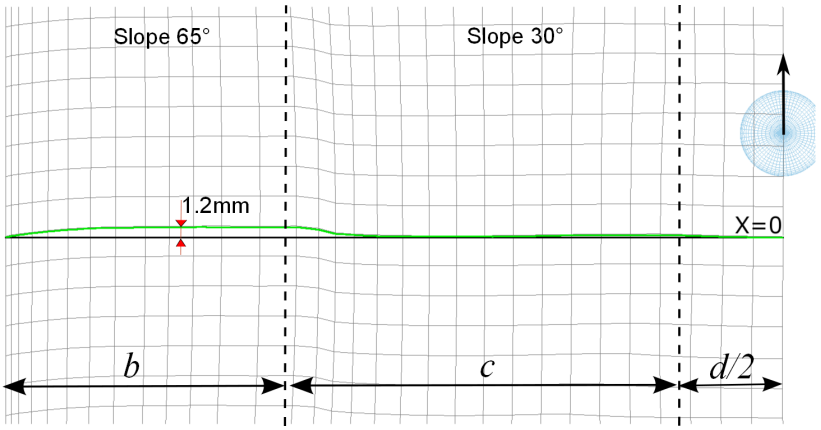


Figure 8: Twist effect at the end of the process for pyramid B. The $x = 0$ black line shows the initial position of the nodes in the undeformed mesh and the green line the final position. The arrow indicates the tool motion direction, with $b$, $c$ and $d$ defined in Fig. 3.

### *4.2. Forces validation*

To simplify the analysis, an average value of the numerical force evolution is considered in each contour (Bouffioux et al., 2010), calculated between points C and D in Fig. 6. The results are presented in Fig. 9, showing a clear difference between the forces when forming the 65° pyramid and the 30° pyramid. In addition to numerical and experimental results, two analytical formulas proposed by Aerens et al. (2009) for the AA3003 are considered. Eq. 6 refers to the the peak force while Eq. 7 refers to the steady force.

$$Fz\_p = 19.1 t^{1.63} d_t^{0.36} \Delta h^{0.09} \alpha \cos\alpha \tag{6}$$

239

$$Fz\_s = 8.35 t^{1.38} d_t^{0.35} \Delta h^{0.09} \alpha \cos\alpha \tag{7}$$

240 where $\Delta h$ is the scallop height related to the step-down $p$ by Eq. 8.

$$p = 2\sin\alpha\sqrt{\Delta h(d_t - \Delta h)} \approx 2\sin\alpha\sqrt{\Delta h d_t} \tag{8}$$

241 In agreement with Aerens et al. (2009), there is no observable peak force for the 30° pyramid.

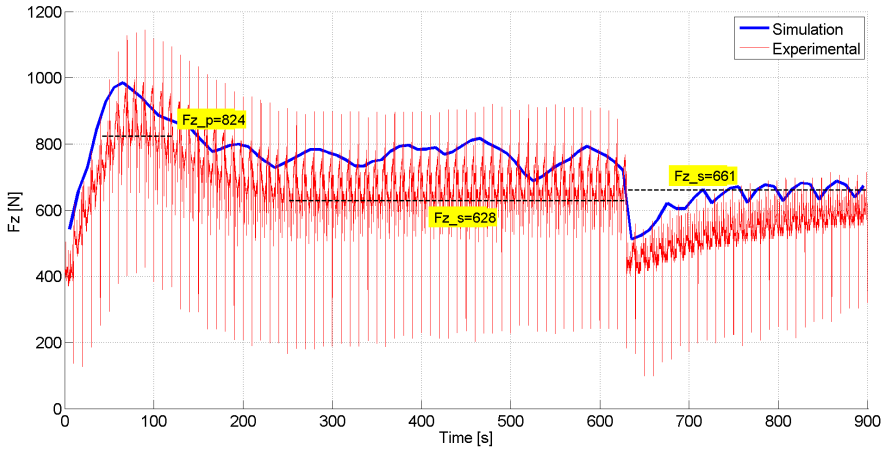


Figure 9: Forming forces in the tool in the $z$ direction when forming the pyramid B.

242

243 In sum and considering both the source of errors and the model's limita-
244 tions, the simulation is able to predict the overall final shape and peak and
245 steady forces. A closer agreement for the shape could be reached by using
246 solid shell elements, where through thickness variables are naturally regarded
247 without hypothesis. The force prediction could be improved in another way,

using more simulations for the material identification or modifying the friction coefficient. For example, removing the friction gives a closer agreement with the measured force (Henrard et al., 2010). Nevertheless, the deviations observed occur mostly due to a bad contact modelling because the localized contact zone cannot be accurately simulated by the chosen mesh density. As demonstrated by Eyckens et al. (2010), good results are obtained using the submodelling technique with brick elements.

## 5. Stress and Strain analysis

In this section, an analysis of the material state is carried out for pyramids A and B. The equivalent plastic strain, von Mises effective stress (see section 3.4) and yield stress are obtained for a cut through $x = 0$, when the tool is in position D (or H) of contour 63 (forming of the 65° pyramid), 75 or 90 (forming of the 30° pyramid). Also the variation through the thickness of the stress components within the sheet plane is analysed. The results are evaluated at the outer integration points.

### *5.1. Equivalent plastic strain analysis*

In order to compare different contours, the results are plotted in Fig. 10 using the initial global reference axis of the undeformed mesh shown in Fig. 5. Also, the tool positions for contours 30, 63 and 75 are shown by shaded orange areas. Looking at Fig. 10(a), it seems that there is not further plasticity in the processed zones when the tool is getting away. Nevertheless, the high value of the equivalent strain prevents the observation of small changes. Hence, a zoom in two different zones were added in order to look for smaller values of plastic strain. In Fig. 10(b), there are plastic strains even

far from the tool contact zone between the contours 63 and 75, and continues to grow until contour 90. Nonetheless, in zone II there are not plastic strains between contour 75 and 90, suggesting that most of the variation between contours 63 and 75 is when the tool is passing in this zone. The strains

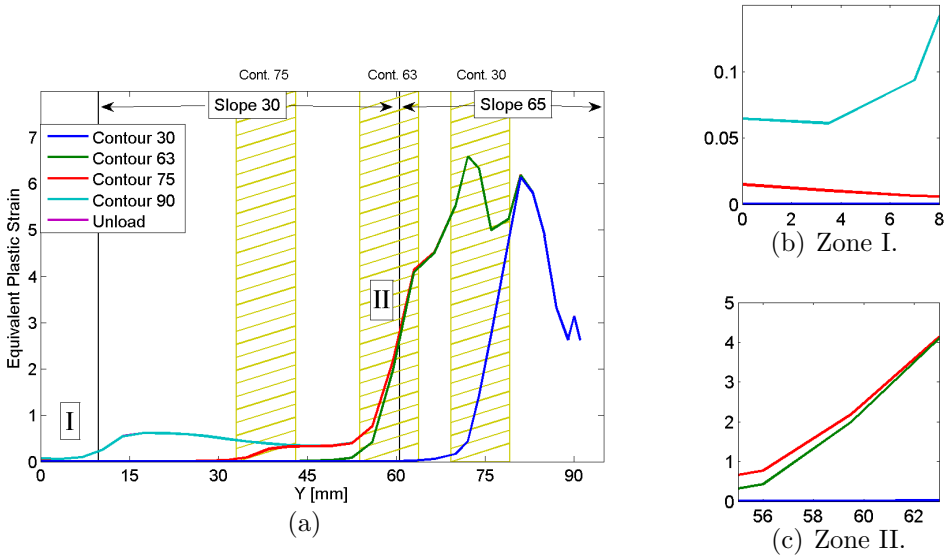


Figure 10: Evolution of the equivalent plastic strain for five contours for the pyramid B. The orange shaded area is the tool position in the contours 30, 63 and 75. Two vertical black lines separate zones for the 30° and the 65° pyramid. Each new curve in the legend is overlapped by the previous one, so the unload step curve is totally under the contour 90 having a negligible effect on the plastic strains.

generated when forming the 65° pyramid are higher than the 30° pyramid, which is explained using the sine law (see for instance, Bambach (2010) for a similar two-slope pyramid).

### *5.2. Stress analysis*

Fig. 11 shows the von Mises effective stress and the yield stress for three different contours. In agreement with the Fig. 10, there is plastic deformation as the tool passes. The level of the yield stress does not increase because of the Voce law, which reaches saturation. In the already processed zone, the von Mises stress is still high even if the tool is far but still lags the yield stress. Considering the close curves of the shape prediction and the experimental measurements, the computed stress fields are assumed reliable. Based in Fig. 10 and Fig. 11, the stresses in zone II produce an elastic response that is mostly structural, i.e. due to the bending moment when the tool is moving further from this zone. The low effect of the unloading step on the strains suggests that the springback is continuously happening during the process and the final shape is both the effect of continuous springback and structural elastic strains.

It is interesting to remark the *U shape* in the stress profile near the center of the pyramid A in the contour 90 Fig. 11(e), which appears when forming the 30° pyramid. The same shape is observed in pyramid B at contour 75 in Fig. 11(d), but it cannot be observed at contour 90 because of the high plastic deformation in the small residual bottom zone. These stresses generates plastic strains in the sheet even in non processed zones and out of the neighbourhood of the tool, as shown in Fig. 10(b). This *U shape* stress is responsible for the small *bulging* observed near the center of the pyramid in Fig. 7.

Despite the bulging, the main geometric deviation from the original CAD occurs in the already processed zone. By looking at Fig. 12(a), it is clear

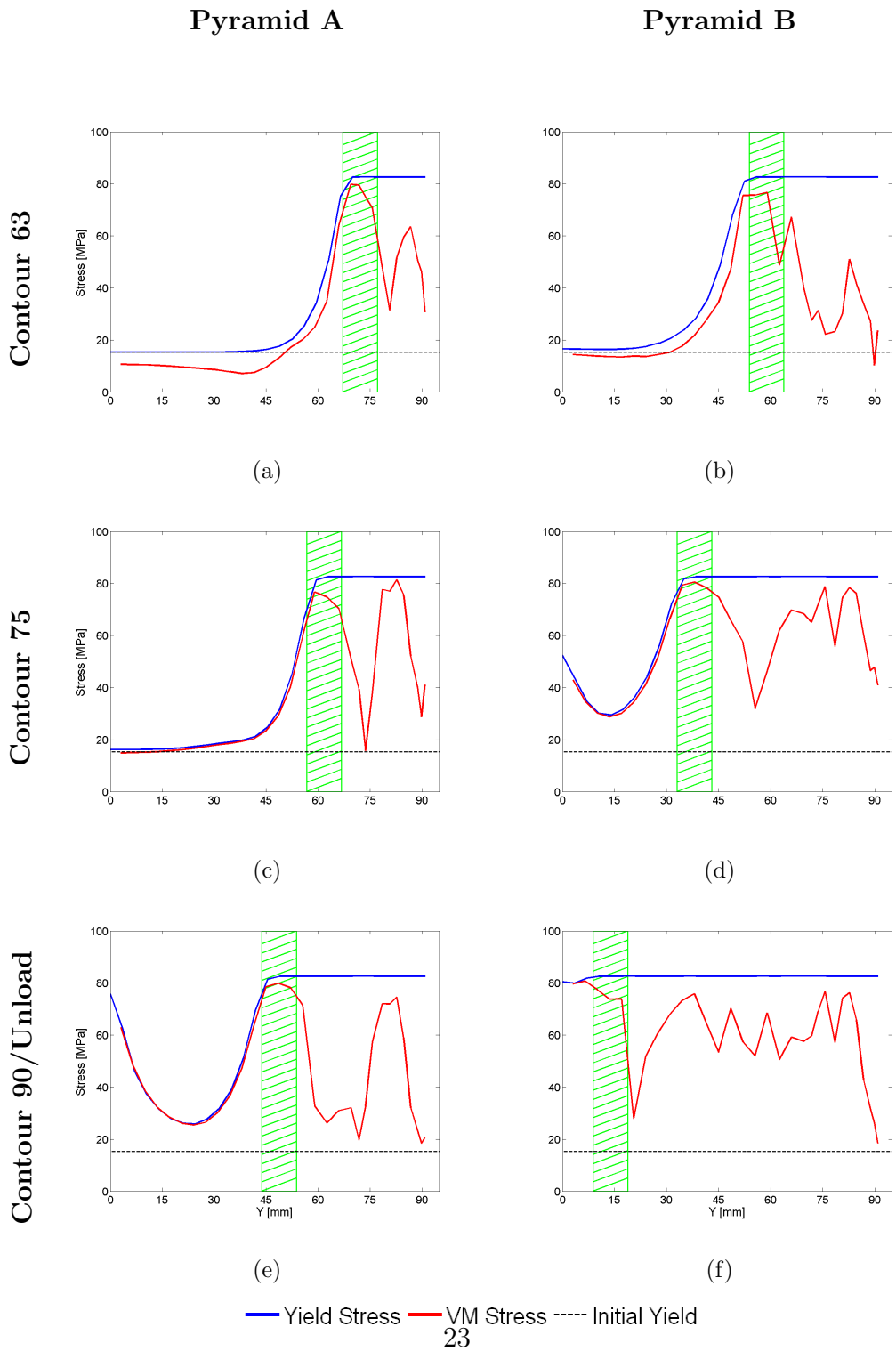




Figure 11: Von Mises effective stress and yield stress for a cut through $x = 0$ for pyramids A and B. The green shaded area defines the tool position. The horizontal dash line is the initial yield stress for the AA3003.

that the displacement of point B when passing from contour 63 to contour 75 is due to a bending moment applied on the previous processed zone. This moment comes from the force $F_z^{75}$ in Eq. 9, which is schematically represented in Fig. 12(b).

$$M_B = F_z^{75} \Delta y \tag{9}$$

Due to the change of angle, the point B is not fixed and is displaced from $B_{63}$ to $B_{75}$. This is the so called *tent effect*, which is dependant of the wall angles and is proportional to the difference between them (Behera et al., 2011). As discussed in section 5.1, no plastic strains are observed in this zone so this effect is purely elastic.

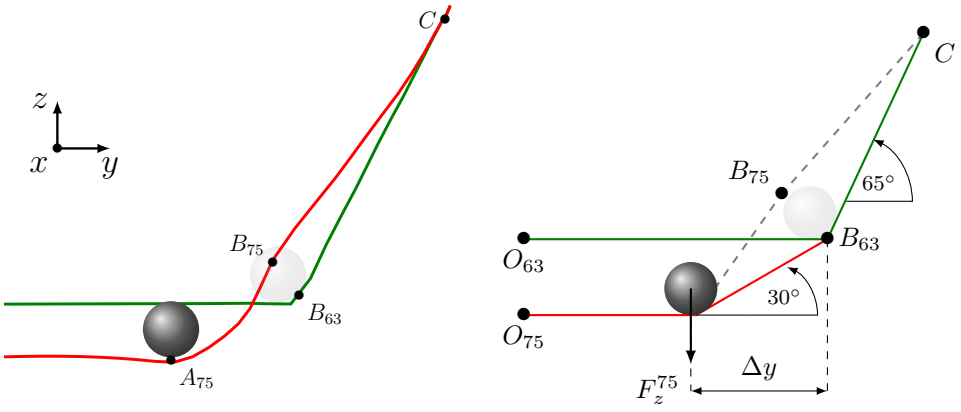


(a) Tent effect. (b) Scheme of the displacement of point B.

Figure 12: Shape deviation when passing from contour 63 to contour 75.

### *5.3. Through thickness stresses analysis*

The local stress components on the local axis of the shell elements are shown in Fig. 14 for three selected elements, depicted in Fig. 13. For contour 65, the element A is closer to the tool and higher stresses are observed. Due to

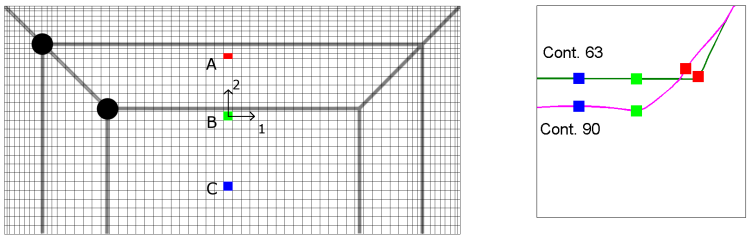


(a) Pyramid A

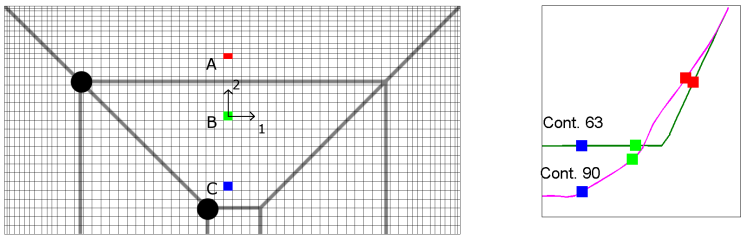


(b) Pyramid B

Figure 13: Position of three selected elements in the initial mesh of the pyramids A and B. The local axis of those elements and the position D and H (Fig. 6) of the tool at the contour 63 and 90 are also depicted.

the shallow shell theory, the element curvature is assumed small and the mid-plane coincides with the neutral plane. Hence, most of the elements in Fig. 14 show a typical bending behaviour in addition to a strong tensile membrane stress in the third integration point. This membrane tension component of element A is also observed in different contours in pyramids A and B, with the notable exception in Fig. 14(h), showing pure bending. The same effect is noticed in the other elements, except element B in Fig. 14(e) in which the membrane component is compression. The bending-under-tension (BUT) is a well known mechanism that is prone to be found in process like stamping. Emmens and van den Boogaard (2009) had previously mentioned it as a stabilization mechanism with the aim to explain the high formability of SPIF process. Jackson and Allwood (2009) also observed the same (plus shear, which is not modelled here). The BUT is a highly localized phenomena, which is however globally reproduced in the simulation.

As tension reduces bending springback (Marciniak et al., 2002), the final shape is due to elastic strains (linked with the *tent effect* in the zone of angle change) and some springback, the latter having just a minor effect in the final shape. This was also observed by Vasilakos et al. (2009), so the main source of geometrical error for this two-slope pyramid does not come from continuous or final springback, as it is commonly believed, but on structural strain related to bending. What is called structural strain is the strain associated with the stress state in element B in Fig. 14(h). The bending effect of axial forces shown in Fig. 12 results in a bending moment applied in a different direction in element B (located in the angle change zone) and in element C. Fig. 10(c) and Fig. 11 confirm that no plastic strain

happens in this change of shape zone after the contour 63.

## 6. Conclusions

In this article, a two-slope SPIF pyramid with two different depths is simulated using the FEM. In order to validate the model, the shape of a transversal cut and the axial force evolution during the process were compared. The model is able to describe correctly the shape despite neglecting the TTS, but the force prediction requires a more precise contact modelling. The use of solid shell elements may lead to an improvement in both predictions.

It is confirmed that there is high dependence of the target geometry on the results with the current toolpath. For instance, even if the equivalent plastic strain distribution through a transversal cut suggest that the plastic deformation is confined to neighbourhood of the tool, a more detailed view shows plastic strains near the center of the pyramid. This plastic strain is also confirmed by looking at the effective von Mises stress, showing values over the initial yield stress in the same zone. Although this could explain the bulging of the center of the pyramid, it is not able to account for the shape deviations in the already formed zones. In those zones, the tent effect is explained by the change of angle which induces a bending moment. This effect is demonstrated to be purely elastic and structural, in the sense that it is due to a change in the moment direction applied in the angle change zone. Moreover, as the variation of stresses during the tool removal is negligible, it is suggested that the springback progressively happens during the forming process. The strong bending behaviour plus membrane tension suggest that most of the

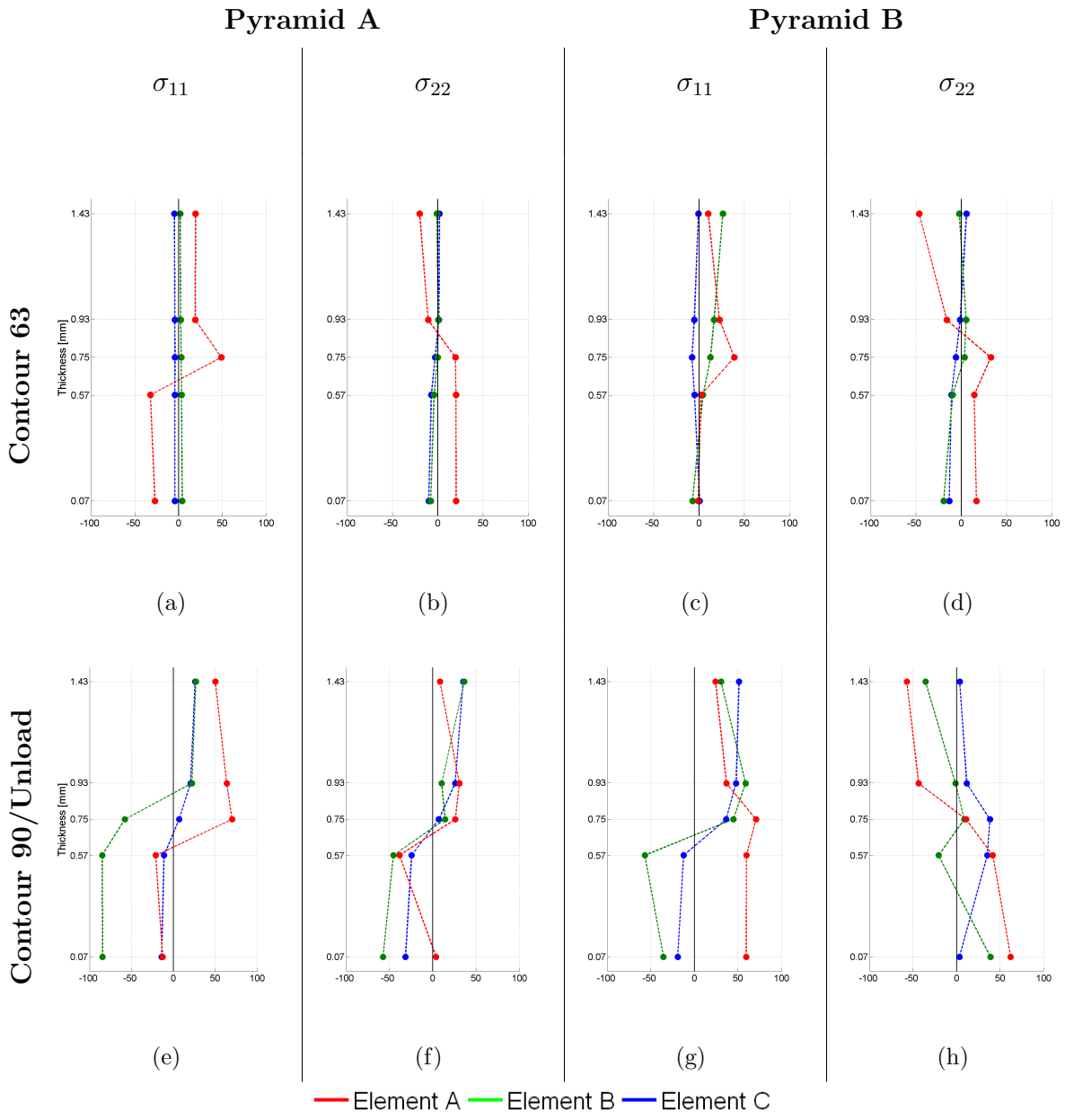


Figure 14: Stress components (in MPa) in local axis through the thickness for the three elements depicted in Fig. 13.

final geometric deviations comes from structural elastic strains related to bending. A further research should consider toolpaths able to decrease the effect of these bending elastic strains in the target CAD geometry.

*Acknowledgements.* The authors acknowledge the Interuniversity Attraction Poles Program PVI 24 and PVII Internal from Belgian Science Policy. C.F. Guzmán and A.M. Habraken also thank the Belgian Fund for Scientific Research FRS-FNRS for its financial support (FRFC-SPIF).

## References

Aerens R, Eyckens P, Van Bael A, Duflou J. Force prediction for single point incremental forming deduced from experimental and FEM observations. The International Journal of Advanced Manufacturing Technology 2009;46(9-12):969–82.

Allwood J, King GPF, Duflou J. A structured search for applications of the incremental sheet-forming process by product segmentation. Proceedings of the Institution of Mechanical Engineers, Part B: Journal of Engineering Manufacture 2005;219(2):239–44.

Ambrogio G, Denapoli L, Filice L, Gagliardi F, Muzzupappa M. Application of Incremental Forming process for high customised medical product manufacturing. Journal of Materials Processing Technology 2005;162-163:156–62.

Ambrogio G, Filice L, Manco GL, Chinesta F, Chastel Y, El Mansori M. Improving process performance in Incremental Sheet Forming (ISF). In:

Chinesta F, Chastel Y, El Mansori M, editors. AMPT. París: American Institute of Physics; 2010. p. 613–8.

Bambach M. Modeling of Optimization Strategies in the Incremental CNC Sheet Metal Forming Process. In: NUMIFORM. AIP; 2004. p. 1969–74.

Bambach M. A geometrical model of the kinematics of incremental sheet forming for the prediction of membrane strains and sheet thickness. Journal of Materials Processing Technology 2010;210(12):1562–73.

Bambach M, Ames J, Azaouzi M, Campagne L, Hirt G, Batoz J. Initial experimental and numerical investigations into a class of new strategies for single point incremental forming simulations. In: Banabic B, editor. ESAFORM. Bucharest; 2005. p. 671–4.

Bambach M, Hirt G. Performance Assessment of Element Formulations and Constitutive Laws for the Simulation of Incremental Sheet Forming (ISF). In: Oñate E, Owen D, editors. COMPLAS. Barcelona: CIMNE; 2005. p. 1–4.

Behera AK, Vanhove H, Lauwers B, Duflou J. Accuracy Improvement in Single Point Incremental Forming through Systematic Study of Feature Interactions. Key Engineering Materials 2011;473:881–8.

Bouffioux C, Pouteau P, Duchêne L, Vanhove H, Duflou J, Habraken AM. Material data identification to model the single point incremental forming process. International Journal of Material Forming 2010;3(S1):979–82.

409 Cescotto S, Grober H. Calibration and application of an elastic viscoplas-
410 tic constitutive equation for steels in hot-rolling conditions. Engineering
411 Computations 1985;2(2):101–6.

412 Duflou J, Callebaut B, Verbert J, De Baerdemaeker H. Improved SPIF per-
413 formance through dynamic local heating. International Journal of Machine
414 Tools and Manufacture 2008a;48(5):543–9.

415 Duflou J, Lauwers B, Verbert J, Tunckol Y, De Baerdemaeker H. Achiev-
416 able Accuracy in Single Point Incremental Forming : Case Studies. In:
417 ESAFORM. Bucharest; volume 2; 2005. p. 675–8.

418 Duflou J, Vanhove H, Verbert J, Gu J, Vasilakos I, Eyckens P. Twist revis-
419 ited: Twist phenomena in single point incremental forming. CIRP Annals
420 - Manufacturing Technology 2010;59(1):307–10.

421 Duflou J, Verbert J, Belkassem B, Gu J, Sol H, Henrard C, Habraken
422 AM. Process window enhancement for single point incremental forming
423 through multi-step toolpaths. CIRP Annals - Manufacturing Technology
424 2008b;57(1):253–6.

425 Emmens W, van den Boogaard A. An overview of stabilizing deformation
426 mechanisms in incremental sheet forming. Journal of Materials Processing
427 Technology 2009;209(8):3688–95.

428 Emmens W, Sebastiani G, van den Boogaard A. The technology of Incre-
429 mental Sheet Forming-A brief review of the history. Journal of Materials
430 Processing Technology 2010;210(8):981–97.

Essa K, Hartley P. An assessment of various process strategies for improving precision in single point incremental forming. International Journal of Material Forming 2010;.

Eyckens P, Belkassem B, Henrard C, Gu J, Sol H, Habraken AM, Duflou J, Bael A, van Houtte P. Strain evolution in the single point incremental forming process: digital image correlation measurement and finite element prediction. International Journal of Material Forming 2010;:55–71.

Eyckens P, Van Bael A, Van Houtte P. An extended Marcini-akKuczynski model for anisotropic sheet subjected to monotonic strain paths with through-thickness shear. International Journal of Plasticity 2011;27(10):1577–97.

Filice L, Fratini L, Micari F. Analysis of Material Formability in Incremental Forming. CIRP Annals - Manufacturing Technology 2002;51(1):199–202.

Flores P, Duchêne L, Bouffioux C, Lelotte T, Henrard C, Pernin N, Van Bael A, He S, Duflou J, Habraken AM. Model identification and FE simulations: Effect of different yield loci and hardening laws in sheet forming. International Journal of Plasticity 2007;23(3):420–49.

Habraken AM, Cescotto S. Contact between deformable solids: The fully coupled approach. Mathematical and Computer Modelling 1998;28(4-8):153–69.

Hadoush A, van den Boogaard A. Substructuring in the implicit simulation of single point incremental sheet forming. International Journal of Material Forming 2009;2(3):181–9.

He S, van Bael A, van Houtte P, Szekeres A, Duflou J, Henrard C, Habraken AM. Finite Element Modeling of Incremental Forming of Aluminum Sheets. Advanced Materials Research 2005;6/8:525–32.

Henrard C. Numerical Simulations of the Single Point Incremental Forming Process. Phd thesis; Université de Liege; 2008.

Henrard C, Bouffioux C, Eyckens P, Sol H, Duflou J, van Houtte P, Van Bael A, Duchêne L, Habraken AM. Forming forces in single point incremental forming: prediction by finite element simulations, validation and sensitivity. Computational Mechanics 2010;47(5):573–90.

Hirt G, Junk S, Witulski N. Incremental sheet forming: quality evaluation and process simulation. In: Proceeding of the 7th ICTP Conference. 2002. p. 925–30.

Jackson K, Allwood J. The mechanics of incremental sheet forming. Journal of Materials Processing Technology 2009;209(3):1158–74.

Jeswiet J, Micari F, Hirt G, Bramley A, Duflou J, Allwood J. Asymmetric Single Point Incremental Forming of Sheet Metal. CIRP Annals - Manufacturing Technology 2005;54(2):88–114.

Jetteur P, Frey F. A four node Marguerre element for non-linear shell analysis. Engineering Computations 1986;3(4):276–82.

Lequesne C, Henrard C, Bouffioux C, Duflou J, Habraken AM. Adaptive remeshing for incremental forming simulation. In: NUMISHEET. Interlaken, Switzerland; 2008. .

476 Marciniak Z, Duncan J, Hu S. Combined bending and tension of sheet. In:
477 Mechanics of sheet metal forming. Butterworth-Heinemann; 2nd ed.; 2002.
478 p. 136–51.

479 Marguerre K. Thermo-elastische Platten-Gleichungen. ZAMM - Journal of
480 Applied Mathematics and Mechanics 1935;15(6):369–72.

481 Micari F, Ambrogio G, Filice L. Shape and dimensional accuracy in Single
482 Point Incremental Forming: State of the art and future trends. Journal of
483 Materials Processing Technology 2007;191(1-3):390–5.

484 Petek A, Gantar G, Pepelnjak T, Kuzman K. Economical and ecological as-
485 pects of single point incremental forming versus deep drawing technology.
486 volume 344. Trans Tech Publ, 2007.

487 Vasilakos I, Gu J, Belkassem B, Sol H, Verbert J, Duflou J. Investigation
488 of Deformation Phenomena in SPIF Using an In-Process DIC Technique.
489 Key Engineering Materials 2009;410-411:401–9.